The following publication Shao, P., Shi, W., & Hao, M. (2018). Indicator-Kriging-Integrated evidence theory for unsupervised change detection in remotely sensed imagery. IEEE Journal of Selected Topics in Applied Earth Observations and Remote Sensing, 11(12), 4649-4663 is available at https://doi.org/10.1109/JSTARS.2018.2878759.

Indicator-Kriging-Integrated Evidence Theory for Unsupervised Change Detection in Remotely Sensed Imagery

Pan Shao, Wenzhong Shi, and Ming Hao

***Abstract*—This study proposes a novel approach based on indicator kriging and Dempster–Shafer (DS) theory for unsupervised change detection in remote sensing images (DSK). Indicator kriging is integrated to the standard DS theory. A feature set with four difference images providing complementary change information is initially generated. Subsequently, the mass functions for each difference image (DI) are determined automatically using fuzzy logic, the four pieces of DI evidence are combined by DS theory, and a preliminary change detection (CD) map is achieved. The preliminary CD map is then divided into three parts adaptively—weakly conflicting part of no change, weakly conflicting part of change, and strongly conflicting part—by calculating the evidence conflict degree for each pixel. Finally, the pixels in the weakly conflicting parts, which have little or no conflict, are labeled as the current class, and the pixels in the strongly conflicting part that contains misclassified pixels are reclassified based on indicator kriging. DSK combines the advantages of different DI features and solves the conflicting situations to a large extent. The main contributions of this work include 1) introducing indicator kriging into CD to manage conflict information during DS fusion and 2) presenting a scheme for producing DI set with complementary change information, developing a novel DSK fusion model for information fusion, and defining the proposed CD framework. Experimental results verify that the proposed DSK is robust and effective for CD.**

***Index Terms*—Remote sensing, unsupervised change detection, Dempster–Shafer theory, indicator kriging, conflict management**

I. INTRODUCTION

The changes occurring on earth surface are considerable environmental characteristics that affect both natural ecosystem and human life [1]. Timely and accurate detection of the changes plays an important role in resource management and sustainable development. Remote sensing images have become a major data source for change detection (CD) because they can be periodically acquired over the same geographical area. In past decades, many CD techniques have been developed and investigated [2], [3]. The techniques are generally partitioned into supervised and unsupervised groups [4].

This study focuses on the most widely used unsupervised CD approaches based on the difference image (DI). From a methodological point of view, DI-based unsupervised CD is usually achieved by three main steps: 1) preprocessing, 2) producing DI between two temporal images, and 3) analyzing the DI. Image preprocessing techniques, like image registration, atmospheric correction, and relative radiometric calibration, are implemented in the first step to make the two considered remotely sensed images comparable in both spatial and spectral domains [5]. The second step compares the two preprocessed images pixel by pixel to produce the DI. In this step, many comparison operators can be applied, including change vector analysis [2], image differencing [2], spectral angle mapper [6], and spectral gradient differencing [7].

In the third step, the DI pixels are classified under changed or unchanged class, by which the CD map is obtained. The problem of distinguishing changed pixels from unchanged ones in the DI can be regarded as an image segmentation problem [8]. The most common method to solve this problem is thresholding. Many known algorithms, like the minimum–error thresholding algorithms based on expectation maximization [4], [9], the Kapur algorithm [10], and the Kittler–Illingworth algorithm [11], can be employed to determine the decision threshold. Techniques of pattern recognition, such as fuzzy C-means (FCM) clustering [12], [13], active contour model [14], fuzzy topology [15], and wavelet transform [16], have been adopted as well to distinguish between changed and unchanged classes.

Although numerous DI-based CD methods have been proposed, no existing method is sufficiently universal to substitute for all others [17], [18]. Selecting the most appropriate algorithm for a given application is difficult. In addition, the accuracy of DI-based CD techniques is always affected by issues such as noise, mixed pixels, overlapping of classes, and limitations of comparison operators (used for producing DI). CD based on a single DI often cannot reach a satisfactory result.

A possible method to solve these problems is to fuse multiple DI features yielded by different algorithms. In doing so, the

Manuscript received; revised; accepted. This work was supported by the National Natural Science Foundation of China (Project No.: 41331175), the Hong Kong Polytechnic University (Project No.: 1_ZVF2 and 1_ZVE8), and the Hubei Engineering Technology Research Center for Farmland Environmental Monitoring (Project No.: 201608 and 201603). (***Corresponding author: Wenzhong Shi***)

Pan Shao is with the Hubei Engineering Technology Research Center for Farmland Environmental Monitoring, China Three Gorges University, Yichang 443002, China. (e-mail: panshao@whu.edu.cn)

Wenzhong Shi is with the Department of Land Surveying and Geo-Informatics, The Hong Kong Polytechnic University, Hung Hom, Hong Kong, China. (e-mail: lswzshi@polyu.edu.hk,).

Ming Hao is with the Key Laboratory for Land Environment and Disaster Monitoring of SBSM, China University of Mining and Technology, Xuzhou, China. (e-mail: haoming@cumt.edu.cn).

peculiarities of different DI-generation algorithms can be synergistically exploited, and, thus a more accurate CD result may be achieved. In remote sensing image analysis, data fusion provides an anticipated tactic for improving the performance and has been studied extensively [19], [20]. Data fusion can be performed at three levels of abstraction closely connected with the flow of data processing: raw data (i.e., pixel), feature, and decision level [19].

In most DI-based CD methods, only one DI is used, although a few studies combine multiple DI images [16]–[18], [21]–[28]. These works can be broadly grouped into two levels: raw data and decision. The former integrates different DIs to a new quality image, which is used for CD afterward, and thus enhances the CD performance. In [21], [22], a log-ratio image and a mean-ratio image were fused using a wavelet transform combination strategy. In [23], a mean-filtered subtraction image and a median-filtered log-ratio image were combined by a weighted average fusion framework. A subtraction image and a ratio image were fused with multiscale wavelet kernels in [16]. A hybrid feature vector (HFV) was constructed using the spectral angle and change vector in [27] to generate DI.

The decision-level fusion group improves CD by fusion of the results obtained from an ensemble of different DI images. Le Hegarat–Mascle *et al*. [18], [26] applied Dempster–Shafer theory (DS) to CD for multiband remotely sensed imagery and fused multi-index CD results. Du *et al*. [17] employed three popular decision-level fusion techniques (i.e., majority voting, DS, and fuzzy integral) to detect urban expansion. Du *et al*. [24] introduced a two-stage sequential fusion CD strategy, which integrates pan-sharpening and decision-level fusion, to fully exploit multi-resolution remote sensing images and various fusion techniques. Zhang *et al*. [25] explored the advantages of combining the results from different CD algorithms and presented a reliability-based fusion CD method. Cai *et al*. [28] proposed an object-oriented CD method for remotely sensed imagery based on adaptive multi-method combination. Liu *et al*. [29] developed a dynamic evidential reasoning (DER) fusion method for CD in remote sensing images. DER was later extended to a more general framework in [30] to deal with heterogeneous images. Tian *et al*. [31] utilized DS theory to combine different change indictors for building CD. Luo *et al*. [32] adopted DS theory to fuse multiple CD methods for urban CD. Liu *et al*. [33] used DS theory to develop noise filter for reducing the false alarms and missing detections. All the aforementioned fusion CD techniques have their own methodological strength, but their robustness and applicability need to be further investigated. How to design a proper fusion model to achieve more accurate and robust CD results remains an open problem [24].

Following the aforementioned works, this study proposes a novel decision-level fusion method to unsupervised CD based on indicator kriging and DS theory, termed as DSK. The rationale of this method is to select typical comparison operators to produce a feature set with four DIs providing complementary change information first. The four DIs are then combined using a properly designed DSK fusion model to obtain the CD map. The proposed DSK CD method has three main characteristics. 1) It combines the CD results obtained from different DI images. 2) It handles the conflicting situations during fusion with special care where the CD results disagree among the DIs. 3) It further introduces the direction and shape change of spectral curves compared with the existing decision–level fusion CD methods, which mainly exploit the magnitude change of spectral values. The two main contributions of this study are as follows:

1. The first introduction of indictor kriging to CD for dealing with conflicts during DS fusion
2. The scheme for producing DI set with complementary change information, the novel DSK fusion model for information fusion, and the framework formulation for the proposed CD method

The remainder of this paper is structured as follows. Section II describes the given scheme for generating DI set. Section III discusses the proposed DSK fusion algorithm in detail. Section IV introduces the datasets used and experimental settings. Section V presents the experimental results on three different real remote sensing images to illustrate the effectiveness of the proposed CD method. Finally, Section VI draws conclusions.

II. GENERATING DIFFERENCE IMAGE SET

As shown in Fig. 1, the proposed method consists of two principal steps: 1) generation of DI set (GDI) and 2) unsupervised fusion based on DSK (UFD). GDI produces four DI images by selecting typical comparison operators, which synchronously consider the magnitude, direction, and shape change between the two temporal images. Then, the four DI features are fused by the DSK algorithm to solve the CD problem.

This section details the step of GDI. Details of the DSK fusion algorithm will be presented in Section III.

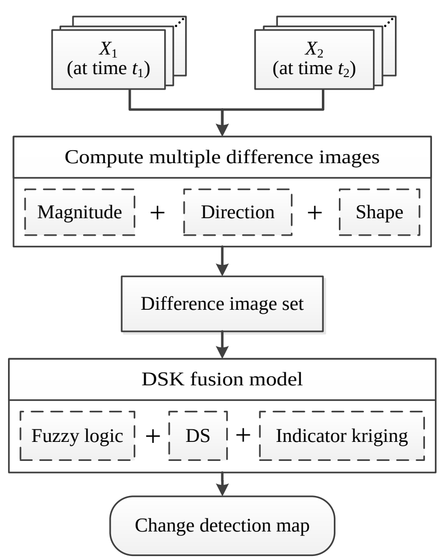

Fig. 1. Block scheme of the proposed DSK CD approach

The essence in using remotely sensed imagery for CD is that changes in land cover will alter the spectral characteristics of earth surface (e.g., reflectance and radiance), which will result in changes in the recorded pixel digital numbers of different temporal images. Different land cover types usually have their own peculiar spectral curves represented by typical spectral values and shapes [7]. For CD, the differences between multitemporal remote sensing images can reflect changes in spectral features indirectly and provide hints to changes in the earth surface during the observation time [17].

Many DI generation algorithms, like image differencing, image ratioing, vegetation index differencing (VID), change vector analysis (CVA), chi-square transformation (CST), principal component analysis (PCA), multivariate alteration detection (MAD), spectral angle mapper (SAM), spectral correlation mapper (SCM), and spectral gradient differencing (SGD), have been proposed to recognize spectral changes [2], [6], [7], [34]. Image differencing uses subtraction to produce DI, which can be performed based on single or multiple image bands [8], [35]. Image ratioing generates the DI by computing the ratio, rather than the difference, between multitemporal images. VID utilizes vegetation indices to identify change information. CVA takes the differences of temporal images in the multidimensional spectrum space and can deal with images with any number of spectral channels. PCA, CST, and MAD exploit data transformation to generate DI images, and the main advantage lies in reducing data redundancy and emphasizing different information in derived components [2]. SAM and SCM describe the differences between two multispectral images from the perspective of direction or angle [6]. SGD employs the spectral gradient for describing spectral shape quantitatively and spectral gradient difference to represent the shape change between spectral curves [7].

A diagrammatic representation of the taxonomy for the main DI generation algorithms is shown in Fig. 2. From the perspective of describing the difference, the algorithms can be divided into those based on magnitude change, direction change, and shape change. The existing methods mainly belong to the first. From a methodological point of view, the algorithms can be grouped into algebra and transformation types. The existing methods mainly belong to the former.

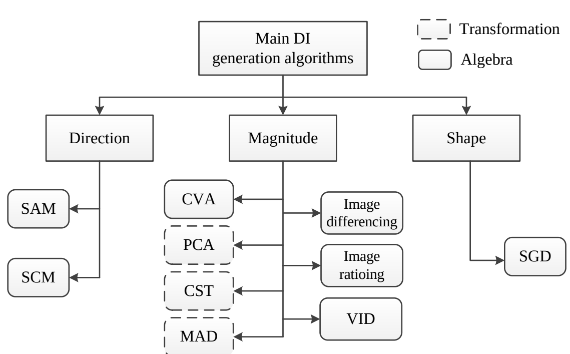

Fig. 2. Taxonomy of main DI generation methods

Two co-registered multispectral remote sensing images X_1 and X_2 of size $I \times J$ are acquired over the same ground area at two different times, t_1 and t_2. Both are composed of B ($B > 1$) spectral bands, and X_l^b is the bth band of X_l, $l = 1, 2$, $b = 1, 2, \ldots, B$.

The first step of the proposed method aims at generating a DI set for X_1 and X_2. A changed pixel may have larger change(s) in magnitude, direction or shape changes [7], [27]. According to these three changing characteristics of the pixels, seven change classes (Table I) may occur in images X_1 and X_2. If any of the three types of change information (magnitude, direction, and shape change) is ignored, some change categories will be missed. For instance, change category 7 cannot be correctly detected if the DI set ignores the shape change. Therefore, the desired DI set should contain all the three types of change information to correctly detect all the seven change classes. In addition, the algebra and transformation algorithms can provide complementary magnitude change [25] and thus are preferably to be both considered for computing the magnitude change.

TABLE I
DIFFERENT CHANGE CATEGORIES

	Change Categories						
	1	2	3	4	5	6	7
With larger magnitude change	√	√	√	×	√	×	×
With larger direction change	√	√	×	√	×	√	×
With larger shape change	√	×	√	√	×	×	√

Given the above analysis, a DI set with four elements is generated, denoted by $S_{DI} = \{DI_1, DI_2, DI_3, DI_4\}$. DI_1 and DI_3 are based on magnitude change, DI_2 based on direction change, and DI_4 based on shape change. DI_1 and DI_3 are computed using the algebra and transformation algorithms, respectively.

DI_1 is defined by the most widely used CVA (algebra) [2], which is essentially Euclidean distance between X_2 and X_1.

$$DI_1 = \sqrt{\sum_{b=1}^{B} \left(X_2^b - X_1^b \right)^2} \tag{1}$$

X_2^b and X_1^b are the bth band of X_2 and X_1, respectively.

DI_2 is generated by SCM [6], which describes the difference between X_2 and X_1 from the perspective of direction. First, the correlation coefficient of X_2 and X_1, denoted by SCM(X_2, X_1), is computed as follows:

$$\mathrm{SCM}(X_2, X_1) = \frac{\sum_{b=1}^{B} \left(X_2^b - \bar{X}_2 \right) \cdot \left(X_1^b - \bar{X}_1 \right)}{\sqrt{\sum_{b=1}^{B} \left(X_2^b - \bar{X}_2 \right)^2} \cdot \sqrt{\sum_{b=1}^{B} \left(X_1^b - \bar{X}_1 \right)^2}},$$

where $\bar{X}_l$ is the mean of spectral bands of image X_l (l = 1, 2). SCM is a centered version of spectral angle mapper (SAM) by the means $\bar{X}_2$ and $\bar{X}_1$ [6]. The value of SCM(X_2, X_1) ranges between -1 and 1. SCM(X_2, X_1) takes the value of -1 when the two vectors are in perfect negative correlation and 1 when they are in perfect positive correlation. SCM(X_2, X_1) is then converted to the correlation distance (i.e., DI_2):

$$DI_2 = 1 - \mathrm{SCM}\left(X_2, X_1 \right) \tag{2}$$

DI_3 is produced based on PCA [2]. Let Cov_R be the covariance matrix of the ratioing change vector $RX = (|1 - X_2^1/X_1^1|, \dots, |1 - X_2^B/X_1^B|)$. Let β_1, β_2, …, β_H be the eigenvalues of Cov_R satisfying $\beta_1 \geqslant \beta_2 \geqslant \cdots \geqslant \beta_H \geqslant 0$; H is the eigenvalue number. Let η_1, η_2, …, η_H be the standard orthogonal eigenvectors corresponding to the eigenvalues β_1, β_2, …, β_H. Then, the hth principal component Y_h for RX can be achieved by the following:

$$Y_h = \eta_h RX^{\mathrm{T}} \quad h = 1, 2, \cdots H \; .$$

T is the transpose operation. DI_3 is then computed by (3), and α_h is the variance contribution rate of the hth principal component.

$$DI_3 = \sum_{h=1}^{H} \alpha_h Y_h, \quad \alpha_h = \frac{\beta_h}{\beta_1 + \beta_2 + \cdots + \beta_H} \tag{3}$$

DI_4 is created with the use of SGD [7]. Let $G_1 = (g_{11}, g_{12}, \dots, g_{1B\text{-}1})$ and $G_2 = (g_{21}, g_{22}, \dots, g_{2B\text{-}1})$ be the spectral gradient vectors from X_1 and X_2, respectively, where

$$g_{lb} = \frac{X_l^{b+1} - X_l^b}{\zeta_{b+1} - \zeta_b}, \quad l = 1, 2, \quad b = 1, 2, \dots, B-1,$$

and ζ_b is the wavelength of band b. Euclidean distance is then applied to G_2 and G_1 to generate DI_4, expressed as follows:

$$DI_4 = \left(\sum_{b=1}^{B-1} \left(g_{2b} - g_{1b} \right)^2 \right)^{1/2} \tag{4}$$

The obtained DIs are then normalized with their pixel values falling in [0, 1] to make the data sets possess the same value range.

III. DSK FUSION ALGORITHM

The proposed DSK fusion algorithm consists of three main steps (Fig. 3). 1) Preliminary fusion step: the four pieces of DI evidence are fused by fuzzy logic and DS theory to achieve a preliminary CD map. 2) Adaptive partition step: the preliminary CD map is divided into three regions adaptively by computing the conflict degree of evidence for each pixel: weakly conflicting region of no change, weakly conflicting region of change, and strongly conflicting region. 3) Indicator kriging step: the pixels in the weakly conflicting region are labeled as the current class, and the strongly conflicting pixel-patterns are reclassified by indicator kriging.

Let w_u and w_c be the unchanged and changed classes. The three steps are detailed in the following subsections.

A. Preliminary fusion step

DS theory initiated from the work of Dempster on the system of probabilities with upper and lower bounds [36] and was later extended by Shafer to a general reasoning framework based on evidence [37]. As an important generalization of the traditional Bayesian theory, DS theory can handle individual as well as composite hypothesis.

DS theory can model both uncertainty and imprecision through the definition of belief (*Bel*) and plausibility (*Pls*) functions, which are derived from a mass (m) function [17]. Let Θ be a frame of discernment and $P(\Theta)$ be the power set of Θ. For any hypotheses A of $P(\Theta)$, $m(A)$ belongs to [0, 1] and satisfies

$$\begin{cases} m(\varnothing) = 0 \\ \sum_{A \in P(\Theta)} m(A) = 1 \end{cases}, \tag{5}$$

where $\varnothing$ designates the empty set and $m(A)$ denotes the mass value of hypothesis A.

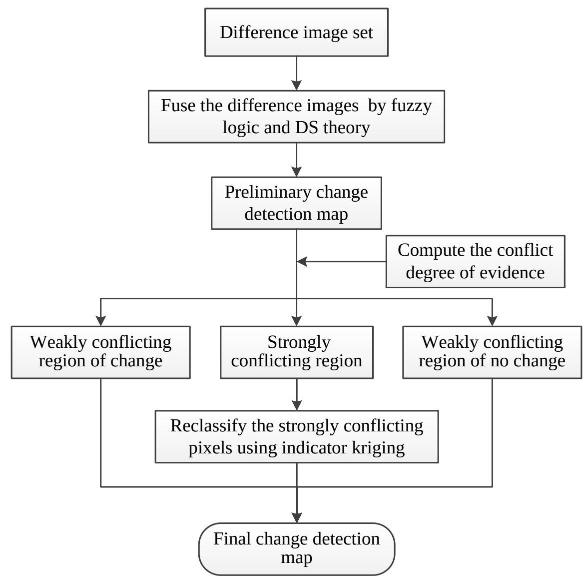

Fig. 3. Flowchart of the proposed DSK fusion model

Consider N evidence with mass functions m_1, m_2, …and m_N, respectively. The joint mass function m can be computed using the Dempster's combination rule [37]:

$$m(A) = \begin{cases} \dfrac{1}{1-\Psi} \sum_{A_1 \cap \cdots \cap A_N = A} \prod_{n=1}^{N} m_n(A_n) & A \neq \varnothing \\ 0 & A = \varnothing \end{cases} \tag{6}$$

with

$$\Psi = \sum_{A_1 \cap \cdots \cap A_N = \varnothing} \prod_{n=1}^{N} m_n(A_n) \tag{7}$$

Ψ denotes the degree of conflict between the evidence, called the conflict coefficient.

In our case, $\Theta = \{w_u, w_c\}$ and $P(\Theta) = \{\varnothing, w_u, w_c, \Theta\}$, where w_u denotes no change and w_c denotes change. Four pieces of evidence are available for Θ, i.e., the four DI images generated in Section II. The first task is to determine a mass function for each DI data to fuse the evidence using DS theory.

Generally, the boundaries of the changed and unchanged classes in DI are not well defined (fuzzy), and the transition between the two classes is smooth. The DI analysis bears inherent fuzziness to a certain extent. Furthermore, operations of assigning pixels to the changed or unchanged class are subjective. Intrinsic uncertainty exists in the DI analysis. Fuzzy clustering is an effective tool to deal with this issue because it can model uncertainty. The DI pixels in fuzzy logic are classified neither to the changed nor the unchanged class but to both classes with certain membership degrees.

Accordingly, this study analyzes the DI images by the concept of fuzzy logic. The most popular fuzzy clustering algorithm FCM is employed to compute the membership functions for each DI. The mass functions of the four pieces of DI evidence are then determined automatically based on the computed FCM membership functions. The details of FCM can be referenced in [38].

Let $U_n = [u_n^i(w_u), u_n^i(w_c)]$ be the membership functions (fuzzy partition matrix) provided by FCM based on the DI_n, n = 1, 2, 3, 4, and $u_n^i(k)$ is the membership grade of pixel p_i to class k obtained from DI_n, meeting the following constraints:

$$\begin{cases} 0 \le u_n^i(k) \le 1, \quad k \in \{w_u, w_c\} \\ u_n^i(w_u) + u_n^i(w_c) = 1 \end{cases} \tag{8}$$

The mass function m_n for evidence DI_n is derived from U_n. Given a pixel p_i, its mass values for the two simple hypotheses w_u and w_c can be defined using its membership degrees $u_n^i(k)$:

$$m_n^i(k) = u_n^i(k) \quad k \in \{w_u, w_c\} \tag{9}$$

where $m_n^i(k)$ denotes the mass value of pixel p_i for hypothesis k according to DI_n. Let $m_n^i(\Theta)$ denote the mass value of pixel p_i for the universal set Θ according to DI_n.

Next, we present the method of defining $m_n^i(\Theta)$. In general, the mass assigned to the universal set Θ is used to describe the imprecision of evidence. For a given pixel p_i, its membership degree set $\pi_n^i = \{u_n^i(w_u), u_n^i(w_c)\}$ (n = 1, 2, 3, 4) is a fuzzy set. The fuzziness of π_n^i can reflect the imprecision in the classification result of pixel p_i obtained from DI_n to a certain extent. Thus, we employ the fuzziness of π_n^i (denoted as E_n^i) to define $m_n^i(\Theta)$:

$$m_n^i(\Theta) = E_n^i \tag{10}$$

The information entropy [39] which is widely used to measure the fuzziness of fuzzy set is applied to compute E_n^i:

$$E_n^i = \frac{-[u_n^i(w_u)\ln(u_n^i(w_u)) + u_n^i(w_c)\ln(u_n^i(w_c))]}{\ln 2} \tag{11}$$

where ln is the natural logarithm operator, and ln2 is a normalization factor to make E_n^i fall in $[0, 1]$.

A scale factor Sca is introduced into (9) and (10) to further improve the mass assignment strategy and control the maximum value of $m_n^i(\Theta)$, expressed as follows:

$$\begin{cases} m_n^i(k) = u_n^i(k) \cdot Sca, \quad k \in \{w_u, w_c\} \\ m_n^i(\Theta) = E_n^i \cdot (1 - Sca) \end{cases} \tag{12}$$

The scale factor Sca is empirically set to 0.7. Finally, the m_n function (n = 1, 2, 3, 4) is such normalized that $m_n^i(\varnothing) = 0$ and $\sum_{k \in P(\Theta)} m_n^i(k) = 1$.

If the reliabilities of the four DI evidence are known, the discounting operation [37] can be applied to the computed mass functions for better fusion performance. Unfortunately, testing samples are unavailable for the considered unsupervised CD problem, thus it is difficult to accurately evaluate the reliabilities of the DI evidence. Given that all the four DI-generation methods have been proved effective, in this study we combine the mass functions with equal weights.

The joint mass function m is computed with the combination rule (6). The joint Bel and Pls functions are then derived from the joint mass function m. A preliminary CD map can be obtained according to the maximum belief procedure. The label L_i for a given pixel p_i is assigned as follows:

$$L_i = \begin{cases} w_u & \text{if } Bel^i(w_u) > Bel^i(w_c) \\ w_c & \text{if } Bel^i(w_u) \le Bel^i(w_c) \end{cases} \tag{13}$$

where $Bel^i(w_u)$ and $Bel^i(w_c)$ denote the joint belief values for p_i on the unchanged and changed classes, respectively.

B. Adaptive partition step

DS theory can integrate multi-source information effectively. However, when the evidence to be fused has strong conflict, the DS theory may result in questionable decisions [20]. Thus, many pixels in the strong conflict region are often misclassified in the preliminary CD map yielded by DS. The preliminary CD result must be further processed to solve this problem. First, the conflict degree between evidence for each pixel is computed and the pixel patterns with strong conflicts (called **strongly conflicting pixels**) are recognized. The recognized patterns are then reclassified using indicator kriging.

Many measurements have been developed to characterize the conflict of evidence, like the conflict coefficient, J distance d_J [40], cosine based distance cos^d [41], and dissimilarity measure $DismP$ [42]. Although the conflict coefficient is not suitable to measure conflicts in some cases [42], [43] and may lead to DSK getting some weak or no conflict pixel patterns, DSK can be tolerant of such an issue to a certain extent thanks to the effective reclassification step. Moreover, the conflict coefficient indicates uncommitted belief [44] and has advantages of finding the pixels whose mass functions have close (or same) beliefs in w_c and w_u. Such pixels are likely to be misclassified due to the similar confidences in w_c and w_u, although they may have weak or no conflicts. Consider two pixels A and B:

A: $m_1(w_u) = 0.5$, $m_1(w_c) = 0.5$; $m_2(w_u) = 0.5$, $m_2(w_c)=0.5$.
B: $m_1(w_u) = 0.51$, $m_1(w_c) = 0.49$; $m_2(w_u)=0.51$, $m_2(w_c)=0.49$.

Then,

$\Psi_A(m_1, m_2) = 0.5$ $\Psi_B(m_1, m_2) = 0.4998$.
$d_{JA}(m_1, m_2) = d_{JB}(m_1, m_2) = 0$.
$cos^d{}_A(m_1, m_2) = cos^d{}_B(m_1, m_2) = 0$.
$DismP_A(m_1, m_2) = DismP_B(m_1, m_2) = 0$.

The pixels A and B are easily to be misclassified because their mass functions have similar confidences in w_c and w_u. The conflict coefficient is more effective in recognizing such easily misclassified pixels compared with the other three conflict measures.

Given the above analysis, in this study the conflict coefficient is employed to measure the conflicts of DI evidence. Following previous studies (e.g. [45]), the conflict among the four pieces of DI evidence is calculated by the average of conflicts between two pieces of evidence. Let Ψ_{gh}^{i} denote the conflict degree between the two pieces of evidence DI_g and DI_h on pixel p_i. It is calculated by the following equation:

$$\Psi_{gh}^{i} = m_g^i(w_u)\cdot m_h^i(w_c) + m_g^i(w_c)\cdot m_h^i(w_u) \qquad (14)$$

where $g\ h = 1, 2, 3, 4$ and $g \neq h$. Equation (14) is the simplified version of (7) for the evidence number is equivalent to 2 and $\Theta = \{w_u, w_c\}$. The total conflict degree Ψ^i between the four pieces of evidence on pixel p_i is evaluated by

$$\Psi^i = \frac{1}{6}\sum_{g=1}^{3}\sum_{h=g+1}^{4}\Psi_{gh}^{i} \qquad (15)$$

The larger the Ψ^i is, the more the four pieces of evidence are conflicting on the pixel p_i. Based on this property, an adaptive thresholding technique is presented to recognize the strongly conflicting pixels.

Let DS_u and DS_c denote the sets of unchanged and changed pixels in the preliminary CD map obtained by DS. Let $\Re^{DS_k}$ be the set made up of the total evidence conflict degrees Ψ^i on the pixels in DS_k. That is $\Re^{DS_k} = \{\Psi^i \mid p_i \in DS_k\}$ and $k \in \{u, c\}$. Let Con^{DS_k} be the set composed of the strongly conflicting pixels in DS_k.

A reasonable strategy for determining the Con^{DS_k} set is to relate it to the statistical features of $\Re^{DS_k}$. Mean and standard deviation are two commonly used statistical parameters that can greatly represent a dataset [8]. The $\Re^{DS_k}$ mean (denoted as $M(\Re^{DS_k})$) and standard deviation (denoted as $Std(\Re^{DS_k})$) are therefore adopted to define the Con^{DS_k} set, expressed as follows:

$$Con^{DS_k} = \left\{p_i \in DS_k \mid \Psi^i > M(\Re^{DS_k}) + T_k \cdot Std(\Re^{DS_k})\right\}, \qquad (16)$$

where T_k is a constant, $k \in \{u, c\}$. The greater the T_k-value is, the fewer elements the set Con^{DS_k} has.

Each class DS_k in the preliminary CD map is partitioned into two parts by (16): strongly conflicting part Con^{DS_k} and weakly conflicting part $Non^{DS_k} = DS_k - Con^{DS_k}$, $k \in \{u, c\}$. As a result, the preliminary CD map is split into three regions: weakly conflicting region of no change Non^{DS_u}, weakly conflicting region of change Non^{DS_c}, and strongly conflicting region $Con^{DS_u} \cup Con^{DS_c}$.

C. Indicator kriging step

The dividing process demonstrates that the pixel patterns in Non^{DS_u} and Non^{DS_c} regions have little or no conflict. The DS theory works well on such patterns, so their preliminary CD results yielded by DS are taken as the final CD results: The pixels in Non^{DS_u} region are finally labeled as the unchanged class, and the ones in Non^{DS_c} region as the changed class. As for the strongly conflicting pixels in $Con^{DS_u} \cup Con^{DS_c}$ region, DS theory often produces problematic results, so these patterns must be reclassified. This study particularly utilizes the indicator kriging to accomplish this task.

Kriging is an interpolation technique to estimate the values of unknown points with observed data, which has been successfully applied in many application areas.

Let $Z(x)$ be a second-order stationary random field with Q observed values $\{Z(x_1), Z(x_2)\ldots, Z(x_Q)\}$, where x_i represents the spatial locations, $i = 1, 2, \ldots, Q$. Then a kriging estimator $Z^*(x_0)$ of the unknown value $Z(x_0)$ can be produced through a linear combination of the observed values:

$$Z^*(x_0) = \sum_{i=1}^{Q}\lambda_i Z(x_i) \qquad (17)$$

where λ_i is the kriging weight denoting the contribution degree of $Z(x_i)$ on $Z^*(x_0)$, $i = 1, 2, \ldots, Q$. The kriging weights $\{\lambda_i\}$ can be determined by solving the kriging system [46].

Ordinary kriging provides an "optimum" estimator of $Z(x_0)$ and estimate error [47]. In our reclassification problem, however, a model providing the probability that a pixel belongs to the unchanged or changed class is more useful than a model giving an estimated value at an unknown location. Indicator kriging, which uses the indicator variables $I_k(x)$ of a random field $Z(x)$ instead of $Z(x)$ itself, provides this capability [48].

We then use indicator kriging to reclassify the strongly conflicting pixels. The main idea is to exploit the class labels of the labeled neighborhood pixels in a window to compute the probabilities that the central pixel (of the window) belongs to the unchanged and changed classes. The window is termed as kriging window.

Let N_i be a neighborhood of pixel p_i. N_i is called a kriging window if it meets the following conditions: 1) p_i does not belong to N_i; and 2) p_i is the center of N_i. Fig. 4 shows an example of a 5×5 kriging window: w_u indicates that the corresponding pixel has been labeled as the unchanged class, w_c represents the corresponding pixel labeled as the changed class, and "none" means that the corresponding pixel is a strongly conflicting pattern that needs to be reclassified.

w_u	w_c	none	w_u	w_u
none	w_c	w_u	none	w_c
w_u	w_u	p_i	w_u	none
w_u	w_c	none	w_u	none
none	w_u	w_c	none	w_u

Fig. 4. Example of a 5×5 kriging window

Let p_{i_0} be a given strongly conflicting pixel. An indicator variable related to the unchanged class w_u, $I_u(\cdot)$, is defined to compute the probability that pixel p_{i_0} belongs to w_u. Indicator values for the pixels labeled as w_u and w_c are set to 1 and 0, respectively. For unlabeled pixels (i.e., the strongly conflicting pixels), which have equal chances to be unchanged and changed, their indicator values are set to ½.

$$I_u(i)=\begin{cases} 1 & \text{if pixel } p_i \in w_u \\ 0 & \text{if pixel } p_i \in w_c \\ 1/2 & \text{if pixel } p_i \text{ is unlabeled} \end{cases} \tag{18}$$

The probability that pixel p_{i_0} belongs to the unchanged class w_u (denoted as $P_u(i_0)$) is estimated as follows [48]:

$$P_u(i_0)=P(p_{i_0}\in w_u)=\sum_{p_i\in N_{i_0}} \lambda_i^{I_u} I_u(i) \tag{19}$$

where N_{i_0} is a kriging window of p_{i_0}, and $\lambda_i^{I_u}$ denote the kriging weights of the pixels in N_{i_0}. The weights { $\lambda_i^{I_u}$ } can be computed by solving the kriging equation of the indicator variable $I_u(\cdot)$:

$$\begin{cases} \sum_{p_j\in N_{i_0}} \lambda_j^{I_u}=1 \\ \sum_{p_j\in N_{i_0}} C^{I_u}\left(p_i - p_j\right)\lambda_j^{I_u} - \ell = C^{I_u}\left(p_i - p_{i_0}\right) \end{cases}, \quad p_i\in N_{i_0} \tag{20}$$

where ℓ is a Lagrange multiplier, $C^{I_u}(p_i - p_j)$ represents the spatial covariance function of the indicator random field $I_u(\cdot)$, and $p_i - p_j$ denotes the spatial distance between the pixels p_i and p_j.

Negative kriging weights obtained by solving (20) may create negative probabilities in (19). A simple and useful scheme is presented to adjust the weights yielded by (20) to avoid such a situation. First, each weight is checked to find the negative weights. The negative ones are then set to 0. Finally, the positive ones are renormalized so that the sum of the weights is equivalent to 1.

The probability that the pixel p_{i_0} belongs to the changed class w_c (denoted as $P_c(i_0)$) can be computed through the same way, in which an indicator variable related to w_c, $I_c(\cdot)$ is defined, and its spatial covariance function $C^{I_c}(p_i - p_j)$ is computed.

The Chebyshev distance is selected to measure the location differences between pixels to reduce the complexity of computing the spatial covariance function. In addition, the indicator variable $I_k(\cdot)$ ($k = u$ or c) is assumed isotropic, and an experimental covariance function $C^{I_k}(p_i - p_j)$ that considers eight directions is calculated for each $I_k(\cdot)$. The eight directions are east, south, west, north, southeast, northeast, southwest, and northwest.

If the size and shape of N_{i_0} do not change, then (20) is independent of pixel p_{i_0}. Equation (20) only needs to be solved once for the unchanged class w_u, and the same coefficients { $\lambda_i^{I_u}$ } are used to compute the probabilities $P_u(i_0)$ for all the strongly conflicting pixels p_{i_0}. This also holds for the changed class.

Two main factors must be considered to determine the kriging window size: Its radius R should be 1) smaller than the correlation "range" of $I_k(\cdot)$ and 2) large enough to provide sufficient labeled pixel patterns. When p_{i_0} is located near the image bounder, N_{i_0} may extend beyond the bounder of the image; to avoid recalculating the kriging equation for a modified N_{i_0}, as done in [47], we assign $I_u(i) = I_c(i) = 0.5$ for the pixels p_i in the unmodified N_{i_0} that locate outside the image.

After the probabilities $P_u(i_0)$ and $P_c(i_0)$ having been estimated for all strongly conflicting pixels p_{i_0}, the maximum probability rule is used to reclassify them. The label L_{i_0} for a given strongly conflicting pixel p_{i_0} is assigned as follows:

$$L_{i_0} = \begin{cases} w_u & \text{if } P_u(i_0) > P_c(i_0) \\ w_c & \text{if } P_u(i_0) \le P_c(i_0) \end{cases} \tag{21}$$

IV. Dataset Description and Experimental Settings

A. Datasets

Three real multispectral remotely sensed images referring to different kinds of changes are used in the experiments to assess the effectiveness of the proposed method. Image preprocessing techniques like radiometric correction, geometric correction, and co-registration have been carried out on the three datasets considered before applying the DSK method. The reference maps (ground truth) are produced manually according to a meticulous visual interpretation of the two original images with the help of ENVI.

The first dataset is the Neimeng dataset, which is made up of two multispectral images acquired by Landsat-5 Thematic Mapper (TM) on August 22, 2006 (t_1) and June 17, 2011 (t_2) on the border of Neimeng and Heilongjiang Provinces, China. An area with 1200×1350 pixels was cropped from the entire available Landsat scene as the test site. Parts of the forest in the considered area were destroyed by a wildfire between the two acquired times. Bands 1–5, and 7 were used for CD. The images of 2006 and 2011 are shown in Figs. 5(a) and (b), and their reference image is shown in Fig. 5(c). Black denotes the unchanged pixels, whereas white denotes the changed pixels.

The second dataset is the Liaoning dataset, which consists of two images taken by the Landsat-7 Enhanced Thematic Mapper Plus (ETM+) sensor on August 11, 2001 (t_1) and August 14, 2002 (t_2) in Liaoning Province, China. The area selected for the experiment is a section with 1100×1500 pixels. The changes occurred mainly because of the new crop planting. Bands 1–4 were used for CD. Figs. 6(a)–(c) show the images of 2001 and

2002 and their reference map, respectively.

The third dataset, the Hunan dataset, comprises two Landsat-8 Operational Land Imager (OLI) images with an area of 3000 ×1600 pixels acquired on September 17, 2013 (t_1) and July 23, 2016 (t_2) in Hunan Province, China. There are roughly four land cover categories in these images (Figs. 7(a) and (b)): water, farmland, building and bare soil, and woodland. The area contains multiple types of change, which were mainly caused by the persistent rain, new crop planting, and urban construction. Bands 1-7 were used for CD.

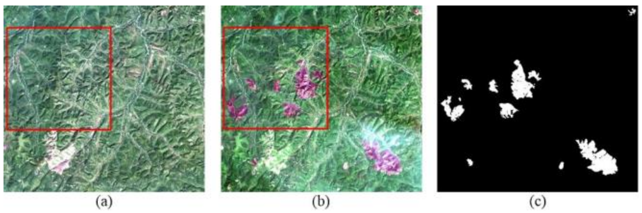

Fig. 5. (a) Landsat-5 TM image of 2006 (RGB (3, 2, 1)), (b) Landsat-5 TM image of 2011 (RGB (3, 2, 1)), and (c) reference map

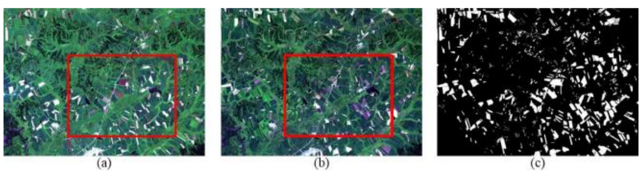

Fig. 6. (a) Landsat-7 ETM+ image of 2001 (RGB (3, 2, 1)), (b) Landsat-7 ETM+ image of 2002 (RGB (3, 2, 1)), and (c) reference map

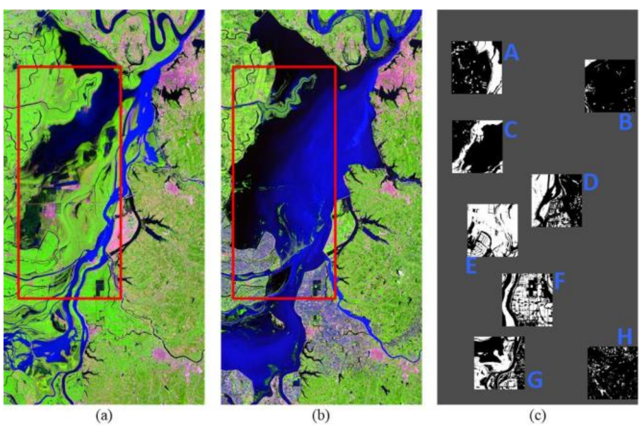

Fig. 7. (a) Landsat-8 OLI image of 2013 (RGB (7, 5, 4)), (b) Landsat-8 OLI image of 2016 (RGB (7, 5, 4)), and (c) reference map

For the third dataset, its larger size and diversity in change aggravate the difficulties in the CD process, and also make it difficult to generate reference map for the whole area. Following [17], sampling technique is used for performance evaluation of Hunan data. To this end, eight image blocks of size 400×400 pixels were selected based on stratified sampling. The blocks include all the kinds of change and have a balanced space distribution. Fig. 7(c) shows the reference images of the eight selected areas.

B. Experiment setup and evaluation criteria

The parameter tests and compared experiments are conducted based on the three considered multispectral remotely sensed datasets to verify the effectiveness of the proposed DSK CD technique.

In the DSK model, two constants, T_u and T_c, determine the thresholds used to recognize the pixels with strong conflicts. The radius R of kriging window determines the window size. Before the compared experiments, how these parameters' values influence the DSK CD results is tested. The test also provides the reasonable parameter values (or ranges) through which better results can be obtained.

The proposed CD method is compared with 1) the ensemble of single-DI detectors based on DI_1 (CVA), DI_2 (SCM), DI_3 (PCA), and DI_4 (SGD) used to produce the input of DSK, and 2) some similar fusion-based approaches: the data-level fusion method based on a hybrid feature vector (HFV), combining SAM and CVA [27], the well-known decision-level fusion techniques DS theory and majority voting rule (MV) [17], as well as the adaptive object-oriented multi-method combination technique (OMC) [28]; and 3) three non-fusion based approaches: the reformulated fuzzy local information C-means (RFLICM) clustering, which is a state-of-the-art fuzzy clustering CD method [22], the FCM clustering incorporating both local and global information (FLGICM) [49], and the trial-and-error (TAE) thresholding (termed as Optimal-T), in which the optimal performance of thresholding is obtained by applying a manual TAE procedure to the reference image of changes. The aim of using Optimal-T as a comparison algorithm is to compare our method with the state-of-the-art thresholding algorithm, such as the method in [35].

The CD results of the four single-DI methods (i.e., DI_1, DI_2, DI_3, and DI_4) are yielded by applying FCM to the DI images separately. In HFV method, after generating the hybrid DI, the changes are detected also by FCM. The RFLICM, FLGICM, and Optimal-T are performed based on DI_1, which is defined by the most widely used CVA. The weighting exponent of FCM, RFLICM, and FLGICM used to control fuzziness degree of membership is set to 2. The other parameters in the comparative algorithms are experimentally explored, and only the best CD results are presented for performance evaluation. In addition, the challenging Hunan data set is taken as an example to analyze the enhancing process of DSK. The impact of image size on different algorithms is analyzed by comparing the CD results from the entire areas and sub-areas in the red rectangles (Figs. 5–7) of the three datasets.

The CD results are analyzed from both visual (qualitative) and quantitative aspects. In the visual analysis, the binary CD map of each method is compared with the binary reference image. Four accuracy indices are then calculated for each CD map to provide the quantitative assessment: 1) missed detections (MD), the number of changed pixels wrongly classified as unchanged ones; 2) false alarms (FA), the number of unchanged pixels wrongly classified as changed ones; 3) overall error (OE), the sum of MD and FA; and 4) Kappa coefficient (KC) [12], [50]. The last two accuracy indices are overall evaluation criteria. KC is reported to be more cogent than OE because more detailed classification information is involved [13]. In addition, the time consumed in the whole process is recorded to compare the computational complexity of different algorithms. The time unit is the second.

V. Experimental results and discussion

A. Test of parameters

This section tests the parameters T_u, T_c, and R to analyze their effect on the DSK CD results and find the appropriate ranges for which relatively high detecting accuracy can be achieved. T_u and T_c are two important parameters of DSK used to recognize strongly conflicting pixels. We set T_k ($k = u$ and c) to {0.5, 1, 1.5, 2, 2.5, 3, 3.5, 4, 4.5, 5, 5.5, 6, 6.5, 7, 7.5, 8} for testing them. The cogent and reliable KC is employed to evaluate the CD results of DSK. Figs. 8(a)–(c) show the relationship between the criterion KC and the parameters T_u and T_c for the three datasets for constant R (taking R = 3). Only part of the testing values is given to show the relationship clearly.

The KC values for the three datasets follow the same tendency with T_u and T_c varying. When the parameter T_u is fixed, the value of KC increases with the T_c-value. On the contrary, when the parameter T_c is fixed, the value of KC decreases as the T_u-value increases. The KC values are stable and best when $T_u \in$ [0.5, 1.5] and $T_c \in$ [6, 8]. That is, we can select any value pair (T_u, T_c) in the region ([0.5, 1.5], [6, 8]) for a reasonable DSK performance for all the three datasets.

The radius R of the kriging window exerts an effect on the final DSK CD result. We set R to 1, 2, 3, 4, and 5 to reveal the relationship between the criterion KC and the parameter R. Fig. 8(d) plots KC against R for the three datasets for constant T_k (taking T_u = 0.5 and T_c = 6). When R changes from 1 to 3, the KC value slowly increases, whereas when R is from 3 to 5, the KC value slightly decreases. The DSK CD results are stable under different R values in the range [1, 5] for all the three datasets used. The stability of KC under various R values shows that DSK is robust for R.

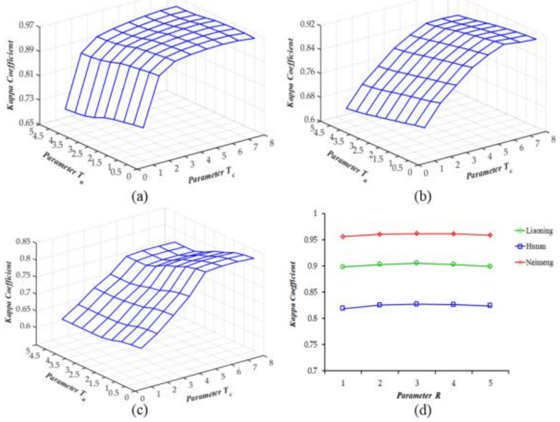

Fig. 8. Relationships between KC and parameters T_u and T_c for (a) Neimeng, (b) Liaoning, and (c) Hunan datasets and (d) relationships between KC and radius R for three datasets

The results with the optimum T_u-, T_c- and R values are given in subsequent compared experiments for performance assessment. Table II lists the T_u, T_c, and R values used in experiments.

TABLE II
VALUES OF THE PARAMETERS USED FOR THE THREE DATASETS

Datasets	Neimeng	Liaoning	Hunan
Parameter values	T_u = 1, T_c = 6, and R = 3	T_u = 0.5, T_c = 6, and R = 3	T_u = 0.5, T_c = 6, and R = 3

B. Results on the Neimeng dataset

We exhibit the experimental results in two ways: the CD maps in figure format and quantitative indices in tabular format. Fig. 9 shows the CD maps obtained from the Neimeng dataset: (a)–(d) are generated by FCM based on DI_1 (CVA), DI_2 (SCM), DI_3 (PCA), and DI_4 (SGD), respectively; (e)–(l) are generated by Optimal-T, RFLICM [22], FLGICM [49], MV [17], DS, HFV [27], OMC [28], and the proposed DSK method. White denotes the changed pixels correctly detected, yellow denotes the false alarms, black denotes the unchanged pixels correctly detected, and red denotes the missed detections. Table III displays the behavior of the four quantitative indices achieved by different algorithms, where the results of the proposed DSK are written in bold.

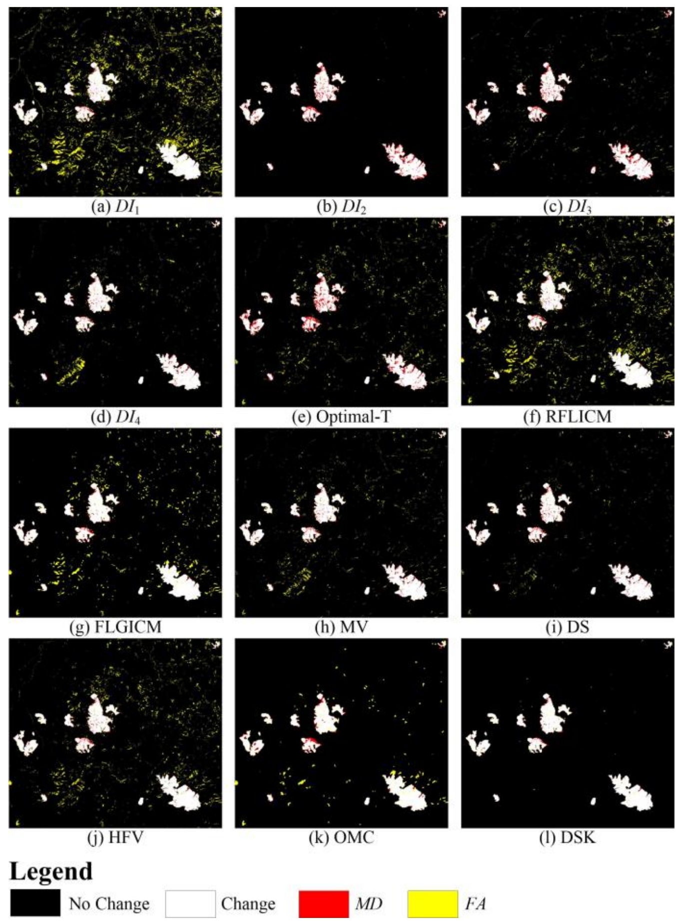

Fig.9. Final CD maps obtained by different methods on Neimeng dataset

As shown in Figs. 9(a)–(d), all the four single-DI detectors can detect most of change information of the Neimeng dataset and they produce different but complementary CD maps. The maps yielded from DI_1 and DI_4 include many yellow scattered noise spots but small red areas (missed detections), whereas the CD map from DI_2 has few yellow false alarms but large red missed detection errors (Table III). This observation shows that it is possible to enhance the performance of individual detectors by using fusion strategies, thereby verifying the rationality of the proposed scheme for generating DI set. The map of DI_2 is the best amongst four single-DI methods for the Neimeng data set.

For the other algorithms, Optimal-T, RFLICM, FLGICM, MV, HFV, and OMC produce better change maps than DI_1, but many false alarms are also detected in their change maps (Figs. 9(e)–(h), (j), and (k)). DS yields similar CD results to DI_2 and better ones than the other comparative methods applied in this work (Table III). The map obtained by DS contains fewer noise spots than those from DI_1, DI_4, Optimal-T, RFLICM, FLGICM, MV, HFV, and OMC, and the missed detection problem is partly solved compared with DI_2 and DI_3 (Figs. 9(a)–(k) and Table III). However, the CD map of DS is not satisfactory enough compared with reference map. Some missed detections and apparent scattered noise spots still exist. The major reason is that though DS works well on weak or no conflict patterns, it often produces problematic fusion results for the patterns with strong conflicts of evidence.

TABLE III
QUANTITATIVE ANALYSIS INDICES FOR CD RESULTS ON NEIMENG DATASET

Methods	*MD*	*FA*	*OE*	*KC*
DI_1	3400	87835	91235	0.6037
DI_2	12280	1174	13454	0.9067
DI_3	11534	7989	19523	0.8708
DI_4	5521	12956	18477	0.8852
Optimal-T	13994	19215	33209	0.7911
RFLICM	4356	53102	57458	0.7099
FLGICM	4000	28412	32412	0.8161
MV	5703	16354	22057	0.8654
DS	6384	8447	14831	0.9049
HFV	4594	31556	36150	0.7975
OMC	6276	12798	19074	0.8809
DSK	**3362**	**2528**	**5890**	**0.9616**

By introducing indicator kriging into DS fusion, the proposed DSK first recognizes the strongly conflicting pixels and then uses the spatial covariance of data to reclassify them. DSK notably improves the DS performance and generates the most accurate CD map (Fig. 9(l)): it removes almost all scattered yellow noise spots in the CD map of DS. Also, the red missed detection area is reduced significantly in the DSK map.

The superiority of the proposed DSK can also be seen from the quantitative analysis indices (Table III). DSK achieves the smallest overall error and the highest Kappa coefficient. The Kappa coefficient value resulted from DSK, 0.9616, has gains between 5.49% and 35.79% compared with all alternative methods.

C. *Results on the Liaoning dataset*

The change maps generated by different methods on Liaoning dataset are shown in Figs. 10: (a)–(d) are obtained by FCM based on the four DI images; (e)–(l) are obtained by Optimal-T, RFLICM, FLGICM, MV, DS, HFV, OMC, and the proposed DSK. Table IV summarizes the four accuracy indices for each CD map.

As seen from Fig. 10 and Table IV, the CD results for the second test dataset are similar to the ones for the Neimeng dataset. The CD maps generated from individual DI images (Figs. 10(a)–(d)) are varied but complementary, which provides the potentials of increasing the CD accuracy of single detectors. The change maps from DI_1 and DI_4 have many yellow noise spots but small missed detection errors (Figs. 10(a) and (d)), whereas the maps of DI_2 and DI_3 contain large missed detection (red) areas but few yellow false alarms (Figs. 10(b) and (c)).

The CD map from DI_4 shows the best performance among the four single-DI methods. For the other seven non-fusion-based and fusion-based algorithms, RFLICM and OMC produce worse CD results, whereas FLGICM, MV, DS, and HFV yield better CD results than those obtained from DI_4 (Figs. 10(f)–(k) and Table IV). However, the maps of FLGICM, MV, and HFV still have many false alarms and the DS map has large red missed detections.

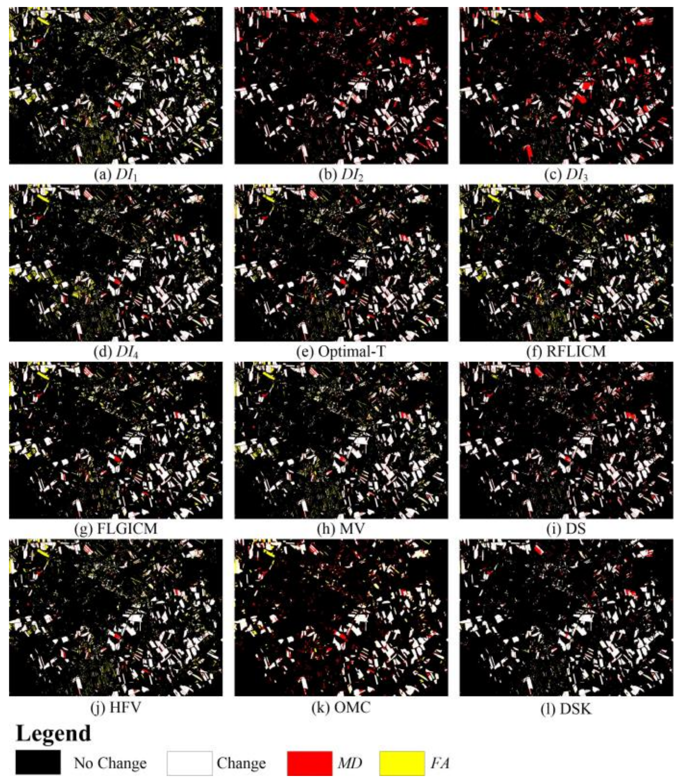

Fig. 10. Final CD maps obtained by different methods on Liaoning dataset

TABLE IV
QUANTITATIVE ANALYSIS INDICES FOR CD RESULTS ON LIAONING DATASET

Methods	*MD*	*FA*	*OE*	*KC*
DI_1	21151	60038	81189	0.7876
DI_2	66165	2765	68930	0.7740
DI_3	68740	7276	76016	0.7519
DI_4	24625	40854	65479	0.8207
Optimal-T	33833	29844	63677	0.8180
RFLICM	23104	47023	70127	0.8109
FLGICM	24396	34886	59282	0.8357
MV	23453	34087	57540	0.8406
DS	39430	8693	48123	0.8540
HFV	22228	38563	60791	0.8336
OMC	46595	22654	69249	0.7932

DSK	**22679**	**9760**	**32439**	**0.9055**

Again, the proposed DSK method outperforms the benchmark methods used in this study and obtains a CD map closest to the reference image (Fig. 10(l)). With respect to the quantitative analysis, DSK demonstrates the lowest overall error and the highest Kappa coefficient. For instance, its overall error is 32439 pixels, which is reduced by at least 15500 pixels compared with the eleven alternative methods.

D. Results on the Hunan dataset

The third experiment is conducted on the Hunan dataset. Fig. 11 displays the CD maps produced by different methods as well as the spatial distribution of the strongly conflicting pixels recognized in DSK. Due to the larger size of Hunan data, the detailed information of CD maps cannot be clearly exhibited in one page. To ease the visual analysis, three typical image blocks are selected for visual comparison. Fig. 12 shows the false color composite images of the three image blocks and their CD maps. Table V reports the quantitative results for the twelve methods computed based on all eight image blocks (Fig 11(n)).

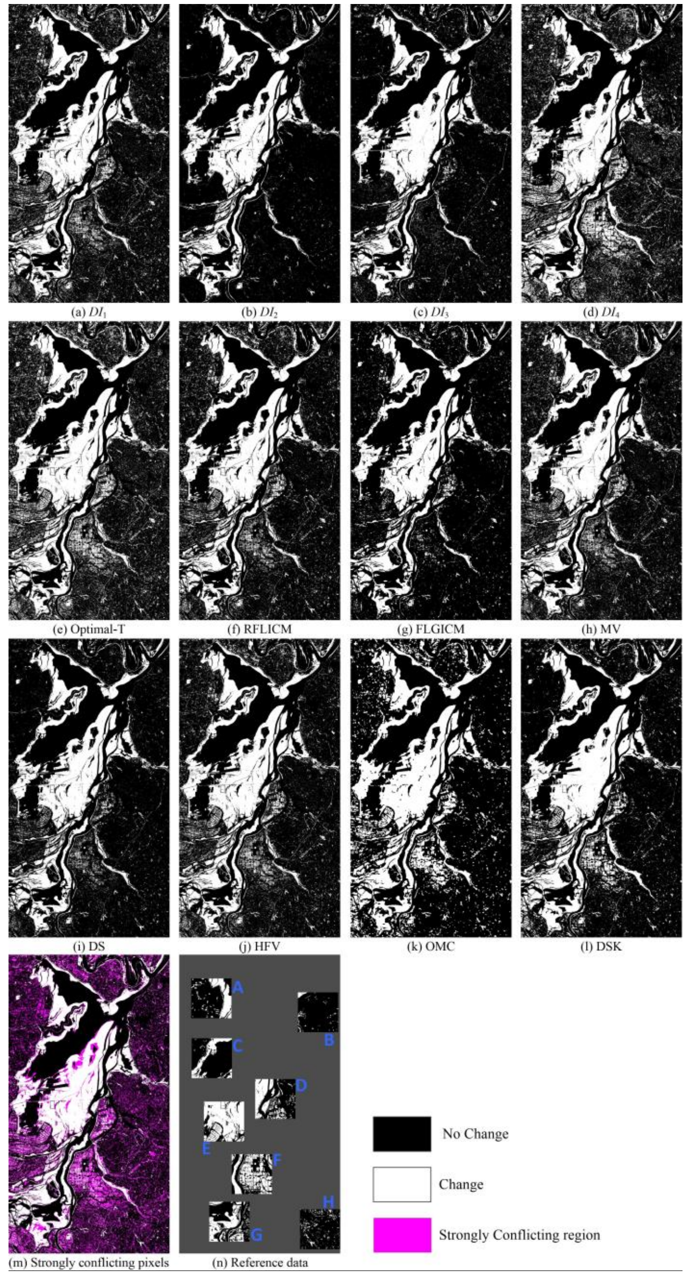

Fig. 11. Final CD maps obtained by different methods on Hunan dataset and spatial distribution of strongly conflicting pixels recognized in DSK

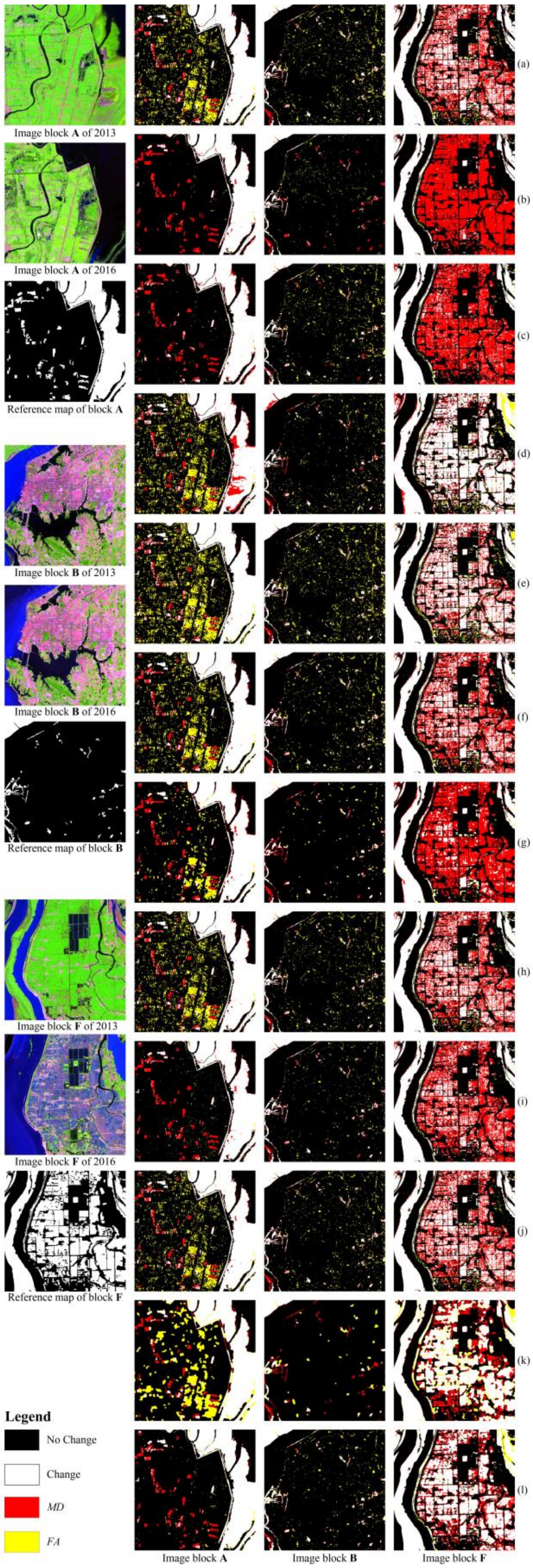

Fig. 12. Image blocks A, B, and F and their CD maps obtained from different methods: (a) DI_1, (b) DI_2, (c) DI_3, (d) DI_4, (e) Optimal-T, (f) RFLICM, (g) FLGICM, (h) MV, (i) DS, (j) HFV, (k), OMC, and (l) the proposed DSK

With reference to Figs. 12(a)─(d), the four single-DI detectors provide complementary change maps; the CD maps obtained from DI_1 and DI_4 contain small missed detections but a number of yellow false alarms, whereas the maps of DI_2 and DI_3 have a little yellow area but large red area. This fact shows the necessity to perform fusion strategy.

As shown in Table V, except RFLICM and FLGICM, the other comparison algorithms produce better CD results than the four single-DI detectors. However, many yellow false alarms are still resulted from Optimal-T, MV, HFV, and OMC (Figs. 12(e), (h), (j) and (k)), and large red missed detection area remains in DS result (Fig. 12(i)). For this challenging data set, the proposed DSK approach also yields the most accurate CD map (Fig. 12(l)).

For the quantitative analysis, DSK has significantly better performance than the eleven benchmark methods, in terms of the decrease of overall error and increase of Kappa coefficient (Table V). For instance, DSK has the highest Kappa coefficient 0.8271, which is 8.09%, 12.34%, 11.29%, 7.65%, 6.00%, 7.73%, 13.75%, 6.68%, 6.62%, 5.52%, and 6.53% larger than DI_1, DI_2, DI_3, DI_4, Optimal-T, RFLICM, FLGICM, MV, DS, HFV, and OMC, respectively. The proposed DSK holds for the same behaviors for the three datasets, and, thus, its robustness can be validated.

TABLE V
QUANTITATIVE ANALYSIS INDICES FOR CD RESULTS ON HUNAN DATASET

Methods	*MD*	*FA*	*OE*	*KC*
DI_1	98603	42243	140846	0.7462
DI_2	149608	6455	156063	0.7037
DI_3	137465	14987	152452	0.7142
DI_4	86756	53509	140265	0.7506
Optimal-T	70010	62914	132924	0.7671
RFLICM	101180	37026	138206	0.7498
FLGICM	147678	17094	164772	0.6896
MV	93986	39105	133091	0.7603
DS	119602	8835	128437	0.7609
HFV	93148	33121	126269	0.7719
OMC	80422	54049	134471	0.7618
DSK	**74742**	**21306**	**96048**	**0.8271**

E. Analysis and discussion

1) Enhancing process of DSK

The three experimental results show that the newly proposed DSK approach yields a comparatively high CD accuracy. As reported in Tables III─V, DSK achieves significantly better results in terms of the Kappa coefficient and overall error, compared with the eleven alternative methods. This is mainly because: 1) as shown in case studies, the four DI images created by the proposed DI-generation scheme can produce different but complementary CD results, providing the potential of improving CD accuracy by fusing these results. 2) DSK is based on DS and inherits its merits on working with the weak conflict pixels. 3) DSK uses indicator kriging to manage conflict information in DS fusion and can improve the CD accuracy on strongly conflicting pixels (Table VI).

In the following paragraphs, the challenging Hunan data is taken as an example to show the effect of using indicator kriging. Fig. 11(m) shows the spatial distribution of the strongly conflicting pixels recognized in DSK. Table VI displays the CD results of different methods on the recognized strongly conflicting pixels, where *OE* is the overall error; *SCOE* and *SCA* are the overall error and detection accuracy, respectively, of the strongly conflicting pixels; and P_{SCOE} denotes the ratio of *SCOE* and *OE*, which is computed with $P_{SCOE} = SCOE/OE \times 100\%$.

TABLE VI
CD RESULTS ON STRONGLY CONFLICTING PIXELS FOR DIFFERENT METHODS

Methods	*OE*	*SCOE*	P_{SCOE}	*SCA*
DI_1	140846	100371	71.26%	0.524
DI_2	156063	88096	56.45%	0.582
DI_3	152452	89080	58.43%	0.577
DI_4	140265	79919	56.98%	0.621
Optimal-T	132924	95556	71.89%	0.546
RFLICM	138206	97094	70.25%	0.539
FLGICM	164772	95563	58.00%	0.546
MV	133091	95459	71.72%	0.547
DS	**128437**	**91580**	**71.03%**	**0.566**
HFV	126269	88364	69.98%	0.581
OMC	134471	69700	51.83%	0.669
DSK	**96048**	**59191**	----	**0.719**

Owing to the diversity of disturbances, complexity of land cover changes, and limitations of comparison operators, many pixels have results where single-DI detectors disagree, as shown in Fig. 11(m). The conflicting pixel patterns are likely to be misclassified in the fusion process. For instance, for Hunan data 91580 misclassified pixels exist in the DS change map, which account for roughly 71% of the DS overall error (128437). The poor capability of handling the strongly conflicting pixels is the main reason for the unsatisfactory CD performance of DS.

By introducing indicator kriging to DS fusion, DSK obtains considerably higher CD accuracy in the recognized strongly conflicting pixels. The CD accuracy of the recognized pixels increases from 56.6% for DS to 71.9% for DSK. As a result, DSK produces the greatest *SCA* amongst all twelve algorithms. In addition, Table VI shows that for all methods, more than half of the misclassified pixels exist in the strongly conflicting area determined by DSK.

2) McNemar's test

McNemar's test [50] is employed to evaluate the statistical significance of differences in CD accuracy for different algorithms. The test follows the standard normal test statistic. The significance of difference between two detectors is:

$$Z_{12} = \frac{f_{12} - f_{21}}{\sqrt{f_{12} + f_{21}}}, \tag{22}$$

where f_{12} is the number of pixels correctly detected by detector 1 but wrongly detected by detector 2, and f_{21} is vice versa. Under the 95% confidence level, if the absolute Z_{12} value is greater than 1.96, then the difference between two CD results is statistically significant.

Table VII shows the McNemar's test results between DSK and the eleven other methods for the three test datasets. The Z_{12} values are computed from all pixels in Neimeng and Liaoning datasets, and the pixels of the eight selected areas (Fig. 11(n)) in Hunan data. Table VII shows that the proposed method can generate statistically significant higher CD results than the benchmark methods applied in this work.

TABLE VII
MCNEMAR'S TEST RESULTS (Z VALUES) BETWEEN DSK AND OTHER METHODS

Detector 1	Detector 2	Neimeng	Liaoning	Hunan
DSK	DI_1	287.33	177.18	149.93
DSK	DI_2	73.65	157.96	193.40
DSK	DI_3	105.45	171.38	189.13
DSK	DI_4	100.15	137.39	128.19
DSK	Optimal-T	156.19	134.21	118.92
DSK	RFLICM	221.71	150.05	146.60
DSK	FLGICM	155.49	118.37	212.32
DSK	MV	116.78	112.87	133.01
DSK	DS	82.28	88.90	133.08
DSK	HFV	166.40	119.82	110.91
DSK	OMC	99.87	144.28	120.83

3) Computational complexity

Table VIII lists the computing time of different algorithms on the three datasets. The "Single-DI detector" column presents the average time of the four single-DI detectors. As shown in Table VIII, single-DI detectors take the least time in each experiment, as they use the classical FCM to perform CD task. Since RFLICM and FLGICM need to compute the spatial term in each iteration, and MV and DS need to repeat FCM four times, they demand more computation time than single-DI detectors. DSK requires some more time than RFLICM, FLGICM, MV, and DS, but much less time than OMC. When we want to obtain more accurate results, it is better to adopt DSK, whereas, when the change maps need producing in shorter time, other methods (except OMC) used in this paper can be exploited. OMC takes the most time as it involves (spatial) feature extraction, image segmentation, and multi-method fusion.

TABLE VIII
COMPUTING TIME OF DIFFERENT ALGORITHMS ON THE THREE DATASETS (S)

	Single-DI detector	RFLICM	FLGICM	MV	DS	HFV	OMC	DSK
Neimeng	15.5	75.1	77.3	65.7	67.4	17.2	178.3	93.8
Liaoning	13.6	68.5	70.8	58.3	59.2	15.5	172.7	86.4
Hunan	39.7	163.6	188.7	125.3	128.5	45.2	421.5	232.1

4) Impact of image size

This subsection analyzes the impact of image size on the CD results. To this end, a sub-area accounting for about a quarter of the whole image, marked by the red rectangles (Figs. 5–7), is selected from each dataset for comparison. The sizes of the sub-regions from Neimeng, Liaoning, and Hunan data are 600 ×700, 600×800, and 1750×800, respectively. Fig. 13 shows the CD results obtained by different algorithms on both the sub-regions and the entire regions.

From Fig. 13, it can be seen that: 1) the proposed DSK yields the smallest overall error and the highest Kappa coefficient for all the entire datasets and sub-regions. 2) Generally, the overall error of the methods increases with the image size, whereas the Kappa coefficient decreases. 3) DSK has the smallest increases in overall error values and the most stable Kappa coefficient as the image sizes increase. In addition, the computing time of the algorithms increases with image size increasing. The speed problem of DSK can be partly solved by parallel computing because the generating and clustering of the four DIs can be carried out at the same time.

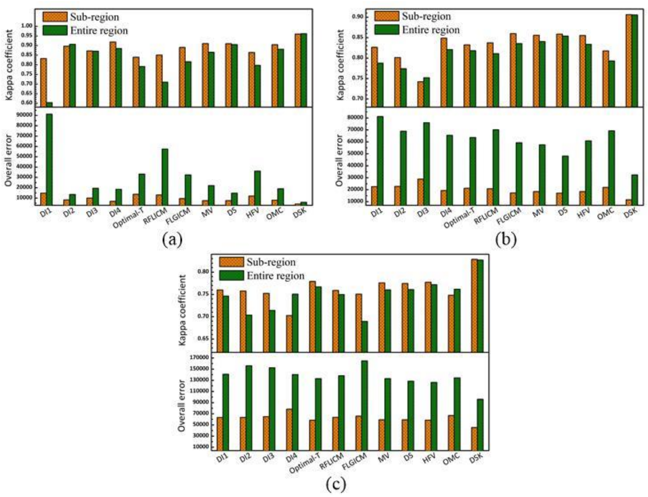

Fig. 13. CD results on the sub-regions and entire regions for (a) Neimeng, (b) Liaoning, and (c) Hunan datasets

5) Future Research

Experimental results show that the proposed DSK approach outperforms the other eleven approaches compared in all three cases, and it can fit different kinds of changes and Landsat images.

In the future work, we will test the DSK CD method in more cases and extend it to other types of remote sensing images, like very high-resolution or synthetic aperture radar (SAR) images. The DSK fusion model can be easily extended to other types of images, but the DI generation scheme needs to be modified according to the characteristics of the used data. For instance, the speckle noises must be considered when extracting DI features for SAR images.

VI. Conclusion

This paper proposes a novel unsupervised CD method for multispectral remote sensing images based on the DSK fusion framework. By selecting typical comparison operators, four DI features are extracted, which simultaneously consider the magnitude, direction, and shape change between spectral curves. The four pieces of DI evidence are fused using fuzzy logic and DS theory, and a preliminary CD map is achieved. The preliminary CD map is then adaptively partitioned into three parts: weakly conflicting part of no change, weakly conflicting part of change, and strongly conflicting part. Finally, the pixels in the weakly conflicting parts are assigned to the current class, and the strongly conflicting pixels are reclassified using indicator kriging, which mainly exploits the spatial correlation of pixels. Therefore, the proposed method can aggregate the CD results from different DIs and largely resolve the conflicting situations where the results disagree.

Three case studies show that the four DI features used can provide different but complementary change information. For all the three experiments, DSK performs better clearly in terms of both qualitative and quantitative measures, compared with the four single-DI detectors and the other seven benchmark methods applied, Optimal-T, RFLICM, FLGICM, MV, DS, HFV, and OMC. These verify the effectiveness and robustness of DSK.

Theoretically, this work contributes to the development of CD by first introducing indicator kriging to solve the conflicting situations in the DS fusion process. Methodologically, this study provides a scheme for generating DI set with complementary change information, proposes a novel DSK fusion model for data fusion, and forms a new CD framework.

An important feature of the proposed DSK method lies in its generalization for fusion in decision level. Four pieces of evidence are used in this study. However, adding or removing evidence in the fusion process is easy. The generality also holds for the inclusion of multiple algorithms. Different algorithms are applied to the same DI image, and the fusion is then done with the results provided by the algorithms. In determining mass functions, other fuzzy clustering like RFLICM can be adopted to substitute for FCM.

Future work will focus on the methods of managing conflicting information and extending the proposed DSK to other types of remotely sensed data, like very high-resolution images.

Acknowledgment

The authors would like to thank Anshu Zhang, Zhewei Liu, and Xianghuan Luo for checking the English. The authors are also grateful to the editors and anonymous reviewers for their valuable comments and suggestions, which greatly improved the quality of this paper.

References

[1] J. Im, J. Rhee, J. R. Jensen, and M. E. Hodgson, “An automated binary change detection model using a calibration approach,” *Remote Sens. Environ.*, vol. 106, no. 1, pp. 89-105, Jan. 2007.

[2] D. Lu, P. Mausel, E. Brondizio, and E. Moran, “Change detection techniques,” *Int. J. Remote Sens.*, vol. 25, no. 12, pp. 2365-2401, Jun. 2004.

[3] M. Hussain, D. Chen, A. Cheng, H. Wei, and D. Stanley, “Change detection from remotely sensed images: From pixel-based to object-based approaches,” *ISPRS J. Photogramm. Remote Sens.*, vol. 80, no. 2, pp. 91-106, Jun. 2013.

[4] L. Bruzzone, and D. F. Prieto, “Automatic analysis of the difference image for unsupervised change detection,” *IEEE Trans. Geosci. Remote Sens.*, vol. 38, no. 3, pp. 1171-1182, May 2000.

[5] L. Bruzzone, and D. F. Prieto, “An adaptive semiparametric and context based approach to unsupervised change detection in multitemporal remote-sensing images,” *IEEE Trans. Image Process.*, vol. 11, no. 4, pp. 452-466, Apr. 2002.

[6] O. A. Carvalho, R. F. Guimaraes, A. R. Gillespie, N. C. Silva, and R. A. T. Gomes, “A new approach to change vector analysis using distance and similarity measures,” *Remote Sens.*, vol. 3, no. 11, pp. 2473-2493, Nov. 2011.

[7] J. Chen, M. Lu, X. Chen, J. Chen, and L. Chen, "A spectral gradient difference based approach for land cover change detection," *ISPRS J. Photogramm. Remote Sens.*, vol. 85, pp. 1-12, Nov. 2013.
[8] P. Shao, W. Z. Shi, P. F. He, M. Hao, and X. K. Zhang, "Novel approach to unsupervised change detection based on a robust semi-supervised FCM clustering algorithm," *Remote Sens.*, vol. 8, no. 3, Mar. 2016.
[9] M. Zanetti, F. Bovolo, and L. Bruzzone, "Rayleigh-Rice Mixture Parameter Estimation via EM Algorithm for Change Detection in Multispectral Images," *IEEE Trans. Image Process.*, vol. 24, no. 12, pp. 5004-5016, Dec. 2015.
[10] S. Patra, S. Ghosh, and A. Ghosh, "Histogram thresholding for unsupervised change detection of remote sensing images," *Int. J. Remote Sens.*, vol. 32, no. 21, pp. 6071-6089, Nov. 2011.
[11] Y. Bazi, L. Bruzzone, and F. Melgani, "An unsupervised approach based on the generalized Gaussian model to automatic change detection in multitemporal SAR images," *IEEE Trans. Geosci. Remote Sens.*, vol. 43, no. 4, pp. 874-887, Apr. 2005.
[12] A. Ghosh, N. S. Mishra, and S. Ghosh, "Fuzzy clustering algorithms for unsupervised change detection in remote sensing images," *Inf. Sci.*, vol. 181, no. 4, pp. 699-715, Feb. 2011.
[13] M. Gong, L. Su, M. Jia, and W. Chen, "Fuzzy clustering with a modified MRF energy function for change detection in synthetic aperture radar images," *IEEE Trans. Fuzzy Syst.*, vol. 22, no. 1, pp. 98-109, Feb. 2014.
[14] M. Hao, W. Shi, H. Zhang, and C. Li, "Unsupervised change detection with expectation-maximization-based level set," *IEEE Geosci. Remote Sens. Lett.*, vol. 11, no. 1, pp. 210-214, Jan. 2014.
[15] W. Z. Shi, P. Shao, M. Hao, P. F. He, and J. M. Wang, "Fuzzy topology-based method for unsupervised change detection," *Remote Sens. Lett.*, vol. 7, no. 1, pp. 81-90, Jan. 2016.
[16] L. Jia, M. Li, P. Zhang, Y. Wu, L. An, and W. Y. Song, "Remote-sensing image change detection with fusion of multiple wavelet kernels," *IEEE J. Sel. Topics Appl. Earth Observ. Remote Sens.*, vol. 9, no. 8, pp. 3405-3418, Aug. 2016.
[17] P. J. Du, S. C. Liu, P. Gamba, K. Tan, and J. S. Xia, "Fusion of difference images for change detection over urban areas," *IEEE J. Sel. Topics Appl. Earth Observ. Remote Sens.*, vol. 5, no. 4, pp. 1076-1086, Aug. 2012.
[18] S. Le Hegarat-Mascle, and R. Seltz, "Automatic change detection by evidential fusion of change indices," *Remote Sens. Environ.*, vol. 91, no. 3/4, pp. 390-404, Jun. 2004.
[19] M. D. Mura, S. Prasad, F. Pacifici, P. Gamba, J. Chanussot, and J. A. Benediktsson, "Challenges and opportunities of multimodality and data fusion in remote sensing," *Proc. IEEE*, vol. 103, no. 9, pp. 1585-1601, Sep. 2015.
[20] B. Khaleghi, A. Khamis, F. O. Karray, and S. N. Razavi, "Multisensor data fusion: A review of the state-of-the-art," *Inf. Fusion*, vol. 14, no. 4, pp. 28-44, Oct. 2013.
[21] J. Ma, M. Gong, and Z. Zhou, "Wavelet fusion on ratio images for change detection in SAR images," *IEEE Geosci. Remote Sens. Lett.*, vol. 9, no. 6, pp. 1122-1126, Nov. 2012.
[22] M. Gong, Z. Zhou, and J. Ma, "Change detection in synthetic aperture radar images based on image fusion and fuzzy clustering," *IEEE Trans. Image Process.*, vol. 21, no. 4, pp. 2141-2151, Apr. 2012.
[23] Y. G. Zheng, X. R. Zhang, B. Hou, and G. C. Liu, "Using combined difference image and k-means clustering for SAR image change detection," *IEEE Geosci. Remote Sens. Lett.*, vol. 11, no. 3, pp. 691-695, Mar. 2014.
[24] P. J. Du, S. C. Liu, J. S. Xia, and Y. D. Zhao, "Information fusion techniques for change detection from multi-temporal remote sensing images," *Inf. Fusion*, vol. 14, no. 1, pp. 19-27, Jan. 2013.
[25] P. Zhang, W. Shi, M. S. Wong, and J. Chen, "A reliability-based multi-algorithm fusion technique in detecting changes in land cover," *Remote Sens.*, vol. 5, no. 3, pp. 1134-1151, Mar. 2013.
[26] S. Le Hegarat-Mascle, R. Seltz, L. Hubert-Moy, S. Corgne, and N. Stach, "Performance of change detection using remotely sensed data and evidential fusion: comparison of three cases of application," *Int. J. Remote Sens.*, vol. 27, no. 16, pp. 3515-3532, Aug. 2006.
[27] H. F. Zhuang, K. Z. Deng, H. D. Fan, and M. Yu, "Strategies Combining Spectral Angle Mapper and Change Vector Analysis to Unsupervised Change Detection in Multispectral Images," *IEEE Geosci. Remote Sens. Lett.*, vol. 13, no. 5, pp. 681-685, May, 2016.
[28] L. Cai, W. Shi, H. Zhang, and M. Hao, "Object-oriented change detection method based on adaptive multi-method combination for remote-sensing images," *Int. J. Remote Sens.*, vol. 37, no. 22, pp. 5457-5471, Nov. 2016.
[29] Z. G. Liu, J. Dezert, G. Mercier, and Q. Pan, "Dynamic evidential reasoning for change detection in remote sensing images," *IEEE Trans. Geosci. Remote Sens.*, vol. 50, no. 5, pp. 1955–1967, May 2012.
[30] Z. G. Liu, G. Mercier, J. Dezert, and Q. Pan, "Change detection in heterogeneous remote sensing images based on multidimensional evidential reasoning," *IEEE Geosci. Remote Sens. Lett.*, vol. 11, no. 1, pp. 168-172, Jan. 2014.
[31] J. J. Tian, S. Y. Cui, and P. Reinartz, "Building change detection based on satellite stereo imagery and digital surface models," *IEEE Trans. Geosci. Remote Sens.*, vol. 52, no. 1, pp. 406-417, Jan. 2014.
[32] H. Luo, C. Liu, C. Wu, and X. Guo, "Urban change detection based on Dempster–Shafer theory for multitemporal very high-resolution imagery," *Remote Sens.*, vol. 10, no. 7, Jun. 2018.
[33] Z. G. Liu, G. Li, G. Mercier, Y. He, and Q. Pan, "Change detection in heterogenous remote sensing images via homogeneous pixel transformation," *IEEE Trans. Image Process.*, vol. 27, no. 4, pp. 1822-1834, Apr. 2018.
[34] M. J. Canty, and A. A. Nielsen, "Linear and kernel methods for multivariate change detection," *Comput. Geosci.*, vol. 38, no. 1, pp. 107-114, Jan. 2012.
[35] M. Zanetti, and L. Bruzzone, "A theoretical framework for change detection based on a compound multiclass statistical model of the difference image," *IEEE Trans. Geosci. Remote Sens*, vol. 56, no. 2, pp. 1129-1143, Feb. 2018.
[36] A. P. Dempster, "Upper and lower probabilities induced by a multivalued mapping," *Ann. Math. Statist.*, vol. 38, no. 2, pp. 325-339, Jun. 1967.
[37] G. Shafer, *A mathematical theory of evidence*. Princeton, NJ, USA: Princeton Univ. Press, 1976.
[38] J. C. Bezdek, *Pattern recognition with fuzzy objective function algorithms*. New York: Plenum, 1981.
[39] K. Brown, G. Foody, and P. Atkinson, "Estimating per-pixel thematic uncertainty in remote sensing classifications," *Int. J. Remote Sens.*, vol. 30, no. 1, pp. 209-229, Jan. 2009.
[40] A. L. Jousselme, D. Grenier, and É. Bossé, "A new distance between two bodies of evidence," *Inf. Fusion,* vol. 2, no. 2, pp. 91-101, Jun. 2001.
[41] A. L. Jousselme, and P. Maupin, "Distances in evidence theory: Comprehensive survey and generalizations," *Int. J. Approx. Reason.*, vol. 53, no. 2, pp. 118-145, Feb. 2012.
[42] Z. G. Liu, J. Dezert, Q. Pan, and G. Mercier, "Combination of sources of evidence with different discounting factors based on a new dissimilarity measure," *Decis. Support Syst.*, vol. 52, no. 1, pp. 133–141, Dec. 2011.
[43] Z. G. Liu, Q. Pan, J. Dezert, J. W. Han, and Y. He, "Classifier fusion with contextual reliability evaluation,"*IEEE Trans. Cybern.*, vol. 48, no. 5, pp. 1605-1618, May 2018.
[44] W. Liu, "Analyzing the degree of conflict among belief functions," *Artif. Intell.*, vol. 170, no. 11, pp. 909–924, Aug. 2006.
[45] Y. Deng, W. K. Shi, Z. F. Zhu, and Q. Liu, "Combining belief functions based on Distance of evidence", *Decis. Support Syst.* vol. 38, no. 3, pp. 489-493, Dec. 2004.
[46] S. Mase, "Geo-Statistics and kriging predictors," in *International Encyclopedia of Statistical Science*, 1st ed., L. Miodrag, Ed. Berlin Heidelberg, Germany: Springer, 2011, pp 609-612.
[47] O. Wonho, and B. Lindquist, "Image thresholding by indicator kriging," *IEEE Trans. Pattern Anal. Mach. Intell.*, vol. 21, no. 7, pp. 590-602, Jul. 1999.
[48] J. L. Chiang, J. J. Liou, C. Wei, and K. S. Cheng, "A feature-space indicator kriging approach for remote sensing image classification," *IEEE Trans. Geosci. Remote Sens.*, vol. 52, no. 7, pp. 4046-4055, Jul. 2014.
[49] M. Hao, H. Zhang, Z. Li, and B. Chen, "Unsupervised change detection using a novel fuzzy c-means clustering simultaneously incorporating local and global information," *Multimedia Tools Appl.*, vol. 76, no. 19, pp. 20081–20098, Oct. 2017.
[50] G. M. Foody, "Thematic map comparison: Evaluating the statistical significance of differences in classification accuracy" *Photogramm. Eng. Remote Sens.*, vol. 70, no. 5, pp. 627-633, May 2004.

Pan Shao is a lecturer in College of Computer and Information Thechnology, China Three Gorges University. He received his doctoral degree in Wuhan University in 2016, China. His research interests include image processing, change detection, and remote sensing image fusion.

Prof Shi is Chair Professor in GISci and remote sensing, Head of Department of Land Surveying and Geo-Informatics, The Hong Kong Polytechnic University. He obtained his doctoral degree from University of Osnabrück in Vechta, Germany in 1994. Prof Shi's current research interests are in the areas of GISci, remote sensing and urban informatics, with focusing on analytics and quality control for spatial big data, object extraction and change detection from satellite images and LiDAR data, integrated indoor mapping technology, 3D and dynamic GISci modelling, and Smart City applications.

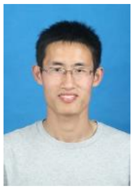

Ming Hao is an associate Professor in remote sensing, Key Laboratory for Land Environment and Disaster Monitoring of SBSM, China University of Mining and Technology. He received his doctoral degree in China University of Mining and Technology in 2015, China. He has authored or coauthored over 20 peer-reviewed articles in international journals such as *Remote Sensing*, *Internatial Journal of Remote Sensing and IEEE Geoscience and Remote Sensing Letters*. His research interests include image processing, information extraction from remote sensing images and remote sensing image fusion.